MOX-Report No. 17/2024

A semi-conservative depth-averaged Material Point Method for fast flow-like landslides and mudflows

Fois, M.; de Falco, C.; Formaggia, L.

MOX, Dipartimento di Matematica
Politecnico di Milano, Via Bonardi 9 - 20133 Milano (Italy)

mox-dmat@polimi.it https://mox.polimi.it

A Semi-Conservative Depth Averaged Material Point Method For Fast Flow-like Landslides and Mudflows

Marco Fois [(1)] Carlo de Falco[(1)] Luca Formaggia[(1)]

February 13, 2024

[(1)] MOX – Modelling and Scientific Computing
Dipartimento di Matematica, Politecnico di Milano
Piazza Leonardo da Vinci, 20133 Milano, Italy
marco.fois@polimi.it
carlo.defalco@polimi.it
luca.formaggia@polimi.it

Keywords: Material Point Method, Landslides modeling, Shallow water, Depth-averaged MPM, Geohazard analysis.

AMS Subject Classification: 35Q35, 35L65, 35Q70, 65Z05, 76D05, 76D99

Abstract

We present a two-dimensional semi-conservative variant of the depth-averaged material point method (DAMPM) for modelling flow-like landslides. The mathematical model is given by the shallow water equations, derived from the depth-integration of the Navier-Stokes equations with the inclusion of an appropriate bed friction model and material rheology, namely Voellmy and the depth-integrated Bingham viscoplastic stress model, respectively. We have verified the validity and performance of the proposed numerical method in different idealised settings and tested its behaviour in a realistic scenario.

1 Introduction and motivations

Among the many types natural disaster that are being made more frequent by climate change, landslides are one of the most dangerous: not only due to their potentially catastrophic impact in terms of human fatalities and economic damage, but also due to their intrinsic unpredictability [1, 2]. Continuous monitoring of areas prone to landslides is imperative. In situ detection systems, such as piezometers and strain gauges, allow accurate monitoring of internal pressures and surface displacements of the area of interest, while satellite surveys can provide detailed topographic and elevation information of the study area [3]. However, empirical monitoring alone is often not sufficient to ensure effective management of an hazardous situation, including preventive capability [4, 5]. The high cost and technical complexity of of realistic experimental analysis therefore warrant the need of developing accurate numerical simulation models for landslides.

The phenomenology of landslides is heterogeneous and consists of several stages. In the initiation phase, the landslide can be modeled as a rigid body subject to gravity, hydrodynamic soil conditions, and pore pressure, which can result in intermittent slides and abrupt changes in velocity. In the run-out phase, in contrast, the landslide material displays a a viscoplastic behaviour and a regime dominated mainly by advection. In this phase, the advancement and evolution of the front depend mainly on the rheology and orography of the area of interest [6]. In many situations, such as debris flows or mudslides, the run-out is characterized by fluid-like behavior and sustained horizontal speeds.

In this work, we focus on the simulation of the evolution of fast-moving landslides immediately after the initiation phase and on the tracking of the advancement front, which is of the utmost importance for predicting the areas which will be impacted and, thus, estimate and/or prevent damages. The basic mathematical model used to describe gravity-driven free surface flows consists of a set of two-dimensional equations, derived from the Navier-Stokes equation for an incompressible fluid by integrating in the vertical direction.

Following the work of [7, 8], we propose a semi-conservative variant of the depth-averaged material point method (DAMPM), which is the depth-integrated version of the Material Point Method (MPM), which originally evolved as an extension of the Particle In Cell (PIC) method [9, 10], and has recently attracted a growing interest for its amenability to acceleration on innovative parallel computing architectures [11, 12].

The use of a depth-averaged formulation for the run-out analysis is useful when considering phenomena occurring over large areas, which would be extremely expensive to simulate with a fully 3D mode [6]. To account in more detail for the effect of the impact of landslides or mudflows on barriers and membranes of complex geometry and smaller characteristic dimensions, we plan in the future to couple the model disussed in this work with 3D particle models for studying impact scenarios [13, 14, 15]. In this context, the equation for the hydrostatic pressure gradient $\frac{1}{2}\rho g \nabla(h^2)$ is also considered in its conservation form and fully integrated into the numerical framework for the management of viscoplastic and fluid-like materials.

The paper is organized as follows. Section 2 is devoted to the presentation of the governing equations, the rheology, and the constitutive models that we adopted to deal with flow-like landslides. We present the complete derivation of the semi-conservative form of the equations

in Section 2.3 and of the numerical method in Section 3. Section 4 deals with numerical experiments, showing some well-balancing and accuracy tests carried out in different idealized scenarios and, in Section 4.3, the results of a simulation of a real test case, namely the Bindo-Cortenova landslide. Finally, Section 5 is devoted to some conclusions and perspectives for future work.

2 Governing equations

We summarize the mathematical model we adopted to deal with flow-like landslides. For a complete derivation, see [16, 17]. We start by making the following assumptions:

A1. The area of interest presents a gentle slope, so we can perform averaging in the vertical direction;

A2. The terrain curvature can be neglected;

A3. The vertical velocities and accelerations are negligible compared with the horizontal counterparts;

A4. The depth of the landslide h is smaller than its horizontal extension.

Let $\Omega \subset \mathbb{R}^2$ be a Cartesian domain and let $(0, T]$ be a time interval with $T > 0$. We consider the conservative form of the depth-averaged equations for the unknown elevation h and linear momentum $h\mathbf{v}$, given by

$$\begin{cases} \partial_t h + \nabla \cdot (h\mathbf{v}) = 0, \\ \partial_t (h\mathbf{v}) + \nabla \cdot \left(\mathbf{v} \otimes h\mathbf{v} + \frac{1}{2} g h^2 \otimes \mathbb{1} \right) = \frac{1}{\rho} \nabla \cdot (h\boldsymbol{\sigma}) + \frac{1}{\rho} \mathbf{B}^f - gh \nabla Z, \end{cases} \tag{1}$$

where $\mathbf{v} = [u, v]^T$ is the horizontal velocity vector, g the gravitational acceleration, ρ the density of the material, assumed constant, $\mathbf{B}^f = [B_x, B_y]^T$ the bed friction, $Z = Z(x, y)$ the orography, and $\boldsymbol{\sigma} = [\sigma_{xx}, \sigma_{yy}, \sigma_{xy}]$ the deviatoric part of the Cauchy stress tensor.

2.1 The rheology

We have enriched the right-hand side of the equation (1) with the bed friction term $\mathbf{B}^f$, following the Voellmy rheology model, that is

$$\mathbf{B}^f = - \left(p^A \tan \varphi + \rho g h \tan \varphi + \frac{\rho g |\mathbf{v}|^2}{\xi} \right) \frac{\mathbf{v}}{|\mathbf{v}|}, \tag{2}$$

where p^A is the atmospheric pressure, φ the friction angle and ξ the turbulence friction acceleration term.

The nature of the phenomena under investigation justifies the combination of a turbulent and a frictional model [18, 19], and this assumption has been shown to produce good results for velocity and deposition during simulations [20].

2.2 The constitutive law

To define the Cauchy stress tensor $\boldsymbol{\sigma}$, we resort to the depth-integrated visco-plastic Bingham stress model, given by

$$\boldsymbol{\sigma} = \left(2\mu + \frac{\tau_Y}{\mathcal{I}_2} \right) \varepsilon. \tag{3}$$

Here, μ is the viscosity of the material, τ_Y the yield shear stress and ε the tensor of the two-dimensional strain rate defined by

$$\varepsilon = \begin{bmatrix} \partial_x u & \frac{1}{2}(\partial_y u + \partial_x v) \\ \frac{1}{2}(\partial_x u + \partial_y v) & \partial_y v \end{bmatrix}.$$

The term $\mathcal{I}_2 = \frac{1}{2}\bar{\varepsilon} : \bar{\varepsilon}$ is the second invariant of the depth-integrated three-dimensional strain rate tensor

$$\bar{\varepsilon} = \begin{bmatrix} \varepsilon_{11} & \varepsilon_{12} & \frac{1}{2}\partial_z u \\ \varepsilon_{21} & \varepsilon_{22} & \frac{1}{2}\partial_z v \\ \frac{1}{2}\partial_z u & \frac{1}{2}\partial_z v & -(\varepsilon_{11} + \varepsilon_{22}) \end{bmatrix},$$

where we have set $\bar{\varepsilon}_{33} = -(\varepsilon_{11} + \varepsilon_{22})$ thanks to the incompressibility constraint.

For the computation of $\mathcal{I}_2$, according to [6, 17], we need to estimate the quantities $\partial_z u$ and $\partial_z v$. To this aim, we exploit the relation for steady-state, laminar, and simple shear fluid.

$$\partial_z \mathbf{v} = \frac{3}{2+\zeta}\frac{\mathbf{v}}{h}, \tag{4}$$

where $\zeta = \tau_Y/\tau_B \in [0, 1]$ and τ_B is the bed resistance force. To estimate the quantity ζ, we use

$$|\mathbf{v}| = \frac{\tau_B}{6\mu}(2+\zeta)(1-\zeta^2). \tag{5}$$

Equation (5) can be rewritten as

$$\zeta^3 + (3+a)\zeta + 2 = 0, \quad \text{with } a = \frac{6\mu|\mathbf{v}|}{\tau_Y h}.$$

We replace the equation of the third degree in ζ with the optimal second-degree approximation, which has a maximum error equal to $1/32$ and is given by

$$48\zeta^2 - (114 + 32a)\zeta + 65 = 0. \tag{6}$$

The equation has two solutions; we take the positive one as the only physically meaningful. Finally, the invariant $\mathcal{I}_2$ can be calculated by replacing the solution of Equation (6) with (4).

2.3 Semi-conservative shallow water system

We derive the semi-conservative form of the system (1) by eleborating the left-hand side of the momentum equations. Without loss of generality, we illustrate only the x-momentum equation.

By using the continuity equation in (1), we may replace the term $\partial_t(h)$ that appears after explicit differentiation, obtaining, after a few simplifications,

$$h\,\partial_t(u) + hu\,\partial_x(u) + hv\,\partial_y(u) + \partial_x\left(\frac{1}{2}gh^2\right) = R.H.S. \tag{7}$$

Note that we have left the pressure term $\partial_x(\frac{1}{2}gh^2)$ in the conservative form.

Now, recalling that $\mathbf{v} = [u, v]^T$ and that

$$\frac{\mathrm{d}u}{\mathrm{d}t} = \partial_t(u) + \mathbf{v}\cdot\nabla u = \partial_t(u) + u\,\partial_x(u) + v\,\partial_y(u), \tag{8}$$

collecting the term h in (7) and moving the pressure term $\partial_x(\frac{1}{2}gh^2)$ at the right-hand-side, we reach the form

$$h\frac{\mathrm{d}u}{\mathrm{d}t} = \frac{1}{\rho}B_x + \frac{1}{\rho}\partial_x\left(\sigma_{xx}h - \frac{1}{2}\rho g h^2\right) + \partial_y(\sigma_{xy}h) - gh\partial_x Z,$$

which is the x-momentum expressed with respect to the material acceleration $\mathrm{d}u/\mathrm{d}t$. At this point, we can multiply all terms by density ρ and merge the x component of the pressure gradient $\partial_x(\frac{1}{2}\rho g h^2)$ with the x component of the tensor $\partial_x(\sigma_{xx}h)$. This leads to

$$\rho h \frac{\mathrm{d}u}{\mathrm{d}t} = B_x + \partial_x \left(\left[\sigma_{xx} - \frac{1}{2}\rho g h \right] h \right) + \partial_y(\sigma_{xy}h) - \rho g h \partial_x Z. \tag{9}$$

The whole procedure can be applied to the y momentum in the same way.

We define an effective stress tensor $\boldsymbol{\sigma}^{\nabla}$ that takes into account the hydrostatic pressure gradient simply as

$$\boldsymbol{\sigma}^{\nabla} = \boldsymbol{\sigma} - \frac{1}{2}\rho g h \otimes \mathbb{1},$$

where $\boldsymbol{\sigma}$ is the Cauchy stress tensor defined in (3) and $\mathbb{1}$ is the unit tensor.

Finally, by setting $\mathbf{b} = -g\nabla Z$ we can rewrite the equation in compact form as

$$\rho h \frac{\mathrm{d}\mathbf{v}}{\mathrm{d}t} = \mathbf{B}^f + \nabla \cdot (\boldsymbol{\sigma}^{\nabla} h) + \rho \mathbf{b} h, \tag{10}$$

and apply the MPM framework, according to [7, 8, 9, 10].

3 Numerical method

Although mesh-based numerical methods, such as the Finite Element Method, are frequently used in the context of free-surface flow simulations [6, 21, 22], these techniques have difficulty dealing with the significant changes in geometry or topology changes typical of landslide phenomena. Moreover, their accuracy is strongly dependent on the quality of the mesh [23].

For this reason, particle-based methods, such as MPM, have gained popularity for the type of simulations we are interested in, where they have been shown to be capable of efficiently managing complex evolving flows and preserving the details of the material front during simulations; see, for example, [24, 25, 26].

3.1 The Depth-Averaged Material Point Method

We provide a detailed derivation of the DAMPM, which is a variant of the Fluid-Implicit Particle (FLIP) and Particle-in-Cell (PIC), originally developed in [10, 27, 9] for continuum mechanical problems.

The first step is to consider the weak form of the momentum equations defined in system (10). For this, we follow the Galerkin procedure and multiply the equation by a sufficiently regular test function ϕ and then integrate it into the domain Ω. Finally, by applying Green's Theorem, we get

$$\int_\Omega \rho h \frac{\mathrm{d}\mathbf{v}}{\mathrm{d}t}\, \phi \, d\mathbf{x} = \int_\Omega (\mathbf{B}^f + \rho \mathbf{b} h)\, \phi \, d\mathbf{x} - \int_\Omega \boldsymbol{\sigma}^{\nabla} h \, \nabla\phi \, d\mathbf{x} + \int_{\partial\Omega} \boldsymbol{\sigma}^{\nabla} h \, \phi \, \mathbf{n} \, d\mathbf{s}, \tag{11}$$

where $\mathbf{n}$ is the outward unit normal to the boundary $\partial\Omega$. Regarding the boundary conditions on (11), we impose a null diffusive interface flux. Moreover, it is also worth noting that the boundary terms do not contribute to the flow as long as the material front does not reach the boundary of the computational domain Ω, which is considered more extensive than the region occupied by the material itself.

3.1.1 Stage 1: Initialization of particles and grid

To discretize (11) we consider the continuum material, i.e. the landslide itself, as a finite collection Ω_p of N_p Lagrangian material points, which represent in this context columns of

material. We define on each particle a mass m_p, which will be kept fixed throughout the simulations, and the initial conditions on every physical quantity necessary to the constitutive model, such as velocities $\mathbf{v}_p$, locations $\mathbf{x}_p$, volumes V_p, areas A_p and stresses $\boldsymbol{\sigma}_p$, for all $p \in \{1, ..., N_p\}$. Following the standard MPM procedure [9, 7, 23], we concentrate the mass m_p on each column by setting

$$\rho h(\mathbf{x}, t) = \sum_{p=1}^{N_p} m_p \delta(\mathbf{x} - \mathbf{x}_p), \ \forall \mathbf{x} \in \Omega, \ \forall t > 0,$$

where $\delta(\mathbf{x} - \mathbf{x}_p)$ is the Dirac delta function. Since we consider the density ρ as constant, we have the following,

$$h(\mathbf{x}, t) = \sum_{p=1}^{N_p} V_p \delta(\mathbf{x} - \mathbf{x}_p), \ \forall \mathbf{x} \in \Omega, \ \forall t > 0, \tag{12}$$

where $V_p = m_p/\rho$. In this way, Equation (11) can be expressed with respect to (12), and it reads

$$\sum_{p=1}^{N_p} m_p \frac{\mathrm{d}\mathbf{v}_p}{\mathrm{d}t} \phi_p = \sum_{p=1}^{N_p} A_p \mathbf{B}_p^f \, \phi_p + \sum_{p=1}^{N_p} \rho V_p \, \mathbf{b}_p \, \phi_p - \sum_{p=1}^{N_p} V_p \boldsymbol{\sigma}_p^{\nabla} \, \nabla \phi_p, \tag{13}$$

where A_p is the area of the column associated with the p^{th} particle and $\phi_p := \phi(\mathbf{x}_p)$.

In order to compute the differential terms in (13), a fixed Eulerian grid is generated to cover the entire physical domain of interest Ω. Grid type can be Cartesian or unstructured, and the most common element shapes used are squares or triangles [23]. Figure 1 shows the typical MPM scheme, with the Eulerian grid and Lagrangian points. In this work, we consider square elements on which we define the standard finite element space $\mathbb{Q}^1(\Omega)$ of continuous piecewise bilinear polynomials. The shape functions in one dimension, say $x-$direction, are given by

$$N_i^x(x) = \begin{cases} 1 - \dfrac{|x - x_i|}{\Delta x} & \text{if } |x - x_i| < \Delta x \\ 0 & \text{otherwise} \end{cases}, \tag{14}$$

where Δx is the element size in the $x-$direction, and x_i is the generic grid node $i \in \{1, ..., N_v\}$. The two-dimensional counterpart is the tensor product of the one-dimensional functions along the two directions, as follows.

$$N_i(x, y) := N_i^x(x) \otimes N_i^y(y). \tag{15}$$

It is important to note that while the use of C^0 basis functions makes calculations easier and more affordable, it can also contribute to the instability of cell crossing due to the presence of discontinuous gradients [23, 28]. This phenomenon, which occurs when a particle crosses from one element to another, can be mitigated by controlling the time step Δt [23]. In this work, we consider

$$\Delta t \leq \mathcal{C} \cdot \frac{\Delta \mathbf{x}}{\max_p \|\mathbf{v}_p\|_2}, \tag{16}$$

where $\mathcal{C}$ is the CFL condition.

Other possibilities, which would, however, increase computational cost and compromise the locality of the problem, are to consider smoother functional spaces by using the B-splines or to resort to more complex MPM formulations, such as the Generalized Interpolation MPM (GIMP). The reader interested in an exhaustive discussion about these variants can refer to [23, 28, 29, 30].

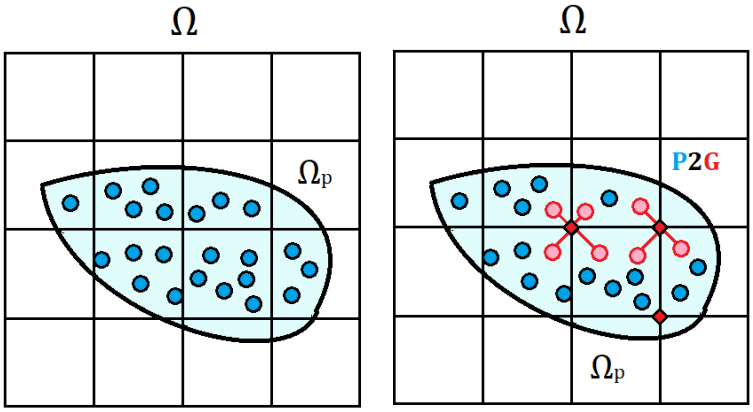

((a)) A Eulerian grid is defined in the domain Ω, while the continuum material is discretized as a set Ω_p of N_p Lagrangian points, each of which has a proper physical property.

((b)) The P2G procedure. The physical quantities defined in the particles are projected, through the basis functions $N_i(\mathbf{x}_p)$, onto the corresponding grid nodes to assemble the nodal forces $\mathbf{F}_i$.

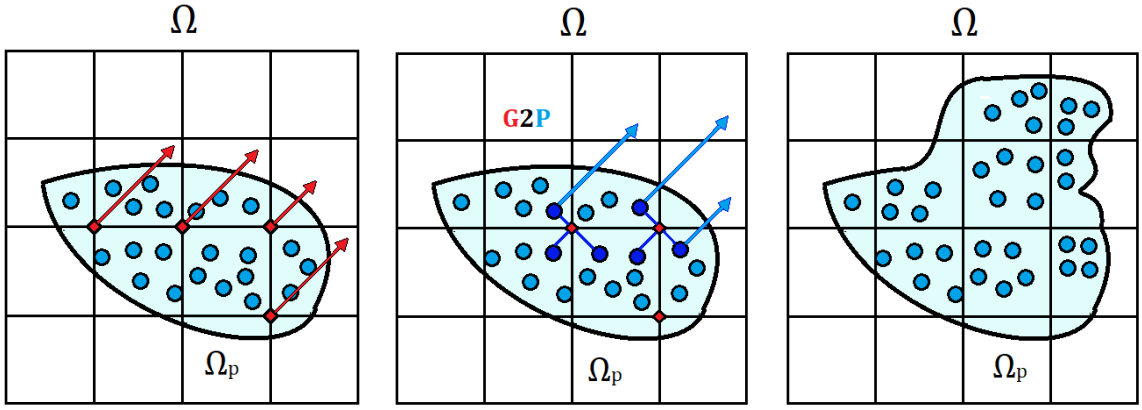

((c)) Advective phase on the grid nodes. Nodal accelerations $\mathbf{a}_i$ and velocities $\mathbf{v}_i$, here depicted with red arrows, are computed by using the nodal masses M_i and the total force $\mathbf{F}_i$.

((d)) The G2P procedure. The advective phase is projected back to the particles.

((e)) Final stage of the method. Once the stresses $\boldsymbol{\sigma}_p^{\nabla}$ are calculated, the particle positions $\mathbf{x}_p$ are updated and the scheme can be started again.

Figure 1: Illustration of the classic MPM algorithm.

.

After the shape functions $N_i(x, y)$ are introduced, we can proceed to the semi-discrete form of the system (10). The particle material acceleration, as well as the test function can be approximated as

$$\mathbf{a}_p := \frac{\mathrm{d}\mathbf{v}_p}{\mathrm{d}t} = \sum_{i=1}^{N_v} \mathbf{a}_i \, N_i(\mathbf{x}_p), \quad \phi_p = \sum_{i=1}^{N_v} \phi_i \, N_i(\mathbf{x}_p), \quad \nabla\phi_p = \sum_{i=1}^{N_v} \phi_i \nabla N_i(\mathbf{x}_p), \tag{17}$$

so that equation (13) becomes

$$\sum_{i=1}^{N_v} \phi_i \cdot \sum_{j=1}^{N_v} M_{ij}\, \mathbf{a}_j = \sum_{i=1}^{N_v} \phi_i \cdot \sum_{p=1}^{N_p} A_p \mathbf{B}_p^f\, N_i(\mathbf{x}_p) + \\ + \sum_{i=1}^{N_v} \phi_i \cdot \sum_{p=1}^{N_p} \rho V_p\, \mathbf{b}_p\, N_i(\mathbf{x}_p) - \sum_{i=1}^{N_v} \phi_i \cdot \sum_{p=1}^{N_p} V_p\, \boldsymbol{\sigma}_p^{\nabla}\, \nabla N_i(\mathbf{x}_p), \quad (18)$$

where M_{ij} is the mass matrix defined by

$$M_{ij} = \sum_{p=1}^{N_p} m_p\, N_i(\mathbf{x}_p)\, N_j(\mathbf{x}_p).$$

Since Equation (18) holds for every sequence $\{\phi_i\}_{i\in\{1,\dots,N_v\}}$,we finally reach the form

$$\sum_{j=1}^{N_v} M_{ij}\mathbf{a}_j \;= \sum_{p=1}^{N_p} A_p \mathbf{B}_p^f\, N_i(\mathbf{x}_p) + \sum_{p=1}^{N_p} \rho V_p \mathbf{b}_p\, N_i(\mathbf{x}_p) - \sum_{p=1}^{N_p} V_p\, \boldsymbol{\sigma}_p^{\nabla}\, \nabla N_i(\mathbf{x}_p), \quad (19)$$

for all $i \in \{1, ..., N_v\}$.

3.1.2 Stage 2: the P2G process

The particle momenta $(m\mathbf{v})_p$ can be projected on the grid nodes as

$$(m\mathbf{v})_i = \sum_{p=1}^{N_p} (m\mathbf{v})_p N_i(\mathbf{x}_p), \quad (20)$$

while the body force $\mathbf{b}_p$, friction $\mathbf{B}_p^f$ and stresses $\boldsymbol{\sigma}_p^{\nabla}$ defined on each particle are used to collect the nodal external and internal forces $\mathbf{F}_i^{\text{ext}}$ and $\mathbf{F}_i^{\text{int}}$, respectively defined as

$$\begin{aligned} \mathbf{F}_i^{\text{ext}} &= \sum_{p=1}^{N_p} \rho V_p\, \mathbf{b}_p N_i(\mathbf{x}_p), \\ \mathbf{F}_i^{\text{int}} &= \sum_{p=1}^{N_p} A_p \mathbf{B}_p^f\, N_i(\mathbf{x}_p) - \sum_{p=1}^{N_p} V_p\, \boldsymbol{\sigma}_p^{\nabla} \nabla N_i(\mathbf{x}_p), \end{aligned} \quad (21)$$

then, by lumping the mass matrix M_{ij} so that

$$M_i \mathbf{a}_i \simeq \sum_{j=1}^{N_v} M_{ij} \mathbf{a}_j,$$

the equation (19) can be essentially written as

$$M_i \mathbf{a}_i = \mathbf{F}_i^{\text{int}} + \mathbf{F}_i^{\text{ext}}, \quad \forall i \in \{1, ..., N_v\}. \quad (22)$$

The total force $\mathbf{F}_i = \mathbf{F}_i^{\text{ext}} + \mathbf{F}_i^{\text{int}}$ collected at the nodes, as shown in Figure 1(b), allows computing the nodal acceleration $\mathbf{a}_i$ and the nodal velocity $\mathbf{v}_i$, by using the lumped mass matrix M_i, as

$$\mathbf{a}_i = \frac{\mathbf{F}_i}{M_i}, \qquad \mathbf{v}_i = \frac{(m\mathbf{v})_i}{M_i}. \quad (23)$$

Finally, the new velocities $\tilde{\mathbf{v}}_v$ are calculated using an explicit time integration scheme directly at the nodes, as shown in Figure 1(c).

$$\tilde{\mathbf{v}}_i = \mathbf{v}_i + \Delta t\, \mathbf{a}_i. \quad (24)$$

3.1.3 Stage 3: the G2P process and particle update

Once the velocities are updated, they are projected back to the particles, to update the positions $\mathbf{x}_p$. To this aim, there are two different ways to compute the projection from nodes to particles: the PIC way and the FLIP way [31].

In the PIC way, the updated particle velocity $\tilde{\mathbf{v}}_p$ is obtained directly from the nodal one, as

$$\tilde{\mathbf{v}}_p = \sum_{i=1}^{N_v} \tilde{\mathbf{v}}_i N_i(\mathbf{x}_p). \tag{25}$$

In the FLIP way, the particle velocity is instead obtained by using the nodal increment, as

$$\tilde{\mathbf{v}}_p = \mathbf{v}_p + \sum_{i=1}^{N_v} (\tilde{\mathbf{v}}_i - \mathbf{v}_i) N_i(\mathbf{x}_p). \tag{26}$$

In this work we chose to follow the PIC way, which, although more dissipative than the FLIP method, it has the advantage of being more stable, according to [23, 31]. With the new particle velocities, is it possible to compute the position update $\tilde{\mathbf{x}}_p$, by using the equation of motion

$$\tilde{\mathbf{x}}_p = \mathbf{x}_p + \Delta t\, \tilde{\mathbf{v}}_p. \tag{27}$$

3.1.4 Stage 4: stresses update and reset

Here we compute the updated particle stresses $\tilde{\boldsymbol{\sigma}}_p^{\nabla}$, following the so-called Update Stresses Last (USL) technique, in which the new stresses are updated, with respect to the constitutive model chosen, only after the nodal velocities $\tilde{\mathbf{v}}_i$ are computed. Therefore, we need to estimate the increase in strain $\Delta\varepsilon_p$, using the grid velocities $\tilde{\mathbf{v}}_i$ just calculated in (24), in such a way that

$$\Delta\varepsilon_p = \frac{\Delta t}{2} \sum_{i=1}^{N_v} \left(\nabla N_i(\mathbf{x}_p)\, \tilde{\mathbf{v}}_i + (\nabla N_i(\mathbf{x}_p)\, \tilde{\mathbf{v}}_i)^T \right). \tag{28}$$

Finally, we estimate the stress increment $\Delta\boldsymbol{\sigma}_p^{\nabla}$, by following the constitutive model shown in Section 2.2, as

$$\tilde{\boldsymbol{\sigma}}_p^{\nabla} = \boldsymbol{\sigma}_p^{\nabla} + \Delta\boldsymbol{\sigma}_p^{\nabla}. \tag{29}$$

Although the USL approach has been shown to be rather dissipative, it is advantageous in terms of stability and convergence compared to other stress update techniques [32, 33].

The last step of the method is to update the depth h_p while satisfying the mass balance defined in (1). Following the work of [7], the updated $\tilde{h}_p$ is given by

$$\tilde{h}_p = \frac{h_p}{1 + \mathrm{tr}(\Delta\varepsilon_p)}. \tag{30}$$

Once the depth of the particles h_p and the positions $\mathbf{x}_p$ are updated, as shown in Figure 1(e), the time is advanced and the nodal variables are reset to zero, to restart the cycle.

4 Numerical Results

The present numerical framework has been applied both in idealized settings and in realistic scenarios. In this Section, we present the numerical results related to some benchmarks well-known in the literature, in which we have investigated the reliability of the proposed method. At the end of the Section, we show the results of the simulation of a real landslide, occurring in Italy in 2002.

4.1 Well-balancing test

The aim of the first test we carried out is to verify that the DAMPM scheme preserves the well-balancing property in the presence of a non-flat bottom. We notice that, to our knowledge, a well-balancing test with the Depth Averaged MPM has never been conducted.

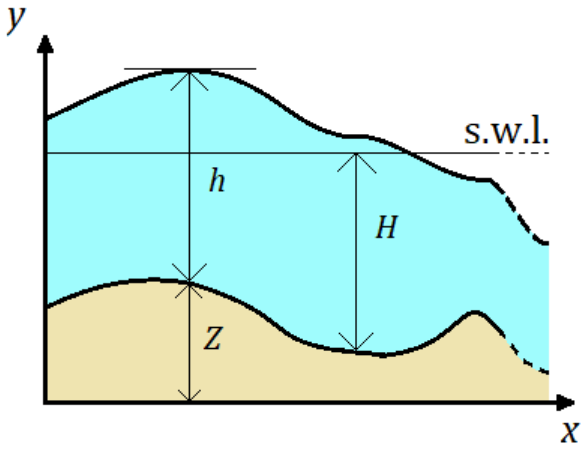

Figure 2: Lake-at-rest problem notation.

To verify the so-called *lake at rest* condition, we choose to perform the test proposed in [17, 34, 35] for a different but equivalent formulation of the system (1), and refer to the "still water level" H, following the notation shown in Figure (2). At first, we notice that, in the steady state, it holds that

$$\nabla H = -\nabla Z. \tag{31}$$

For the sake of simplicity, we refer to the $x-$momentum equation of (1) and consider the term $-gH\,\partial_x Z$ on the right-hand side. By replacing it with (31) and by adding and subtracting the term $gH\,\nabla H$, equation (1) becomes

$$\begin{aligned} L.H.S. &= \frac{1}{\rho}\left[\nabla\cdot(h\boldsymbol{\sigma}) + \mathbf{B}^f\right] + gH\,\nabla H - gH\,\nabla H + gh\,\nabla H \\ &= \frac{1}{\rho}\left[\nabla\cdot(h\boldsymbol{\sigma}) + \mathbf{B}^f\right] + \frac{1}{2}g\nabla(H^2) + g(h-H)\nabla H. \end{aligned} \tag{32}$$

The new formulation can be reached by moving the term $1/2g\nabla(H^2)$ on the left-hand-side of (32), by merging it with the hydrostatic pressure gradient and by using again (31), in such a way that

$$\partial_t(h\mathbf{v}) + \nabla\cdot\left(\mathbf{v}\otimes h\mathbf{v} + \frac{1}{2}g(h^2-H^2)\otimes\mathbb{1}\right) = \frac{1}{\rho}\mathbf{B}^f + \frac{1}{\rho}\nabla\cdot(h\boldsymbol{\sigma}) - g(h-H)\nabla Z. \tag{33}$$

We notice that the entire numerical framework proposed in Section (3) can be applied in an analogous fashion to the new formulation, which is, unfortunately, useful only as long as the still water level H is available.

Following the works [36, 37], we have performed the well-balancing test on two different orthographies $Z_1(x,y)$ and $Z_2(x,y)$, respectively defined by

$$Z_1(\mathbf{x}) = 5\exp\left(-\frac{2}{5}\|\mathbf{x}-5\|^2\right), \qquad Z_2(\mathbf{x}) = \begin{cases} 4 & \text{if } \mathbf{x}\in[4,8]^2 \\ 0 & \text{otherwise} \end{cases}. \tag{34}$$

The computational domain is defined by $\Omega = [0,10]^2$, and the initial conditions are set to coincide with the steady solutions, given by

$$\begin{aligned} &h(\mathbf{x},t) + Z_i(\mathbf{x}) = 10, \\ &u(\mathbf{x},t) = v(\mathbf{x},t) = 0, \end{aligned} \qquad \forall t\in(0,T],\ \mathbf{x}\in\Omega,\ i=1,2, \tag{35}$$

while the final time is set to $T = 1\,s$. The domain Ω is discretised with a grid consisting of 2500 elements and a total of 10000 material points, that is, 4 particles per cell. This test was carried out in the absence of friction in the whole domain Ω.

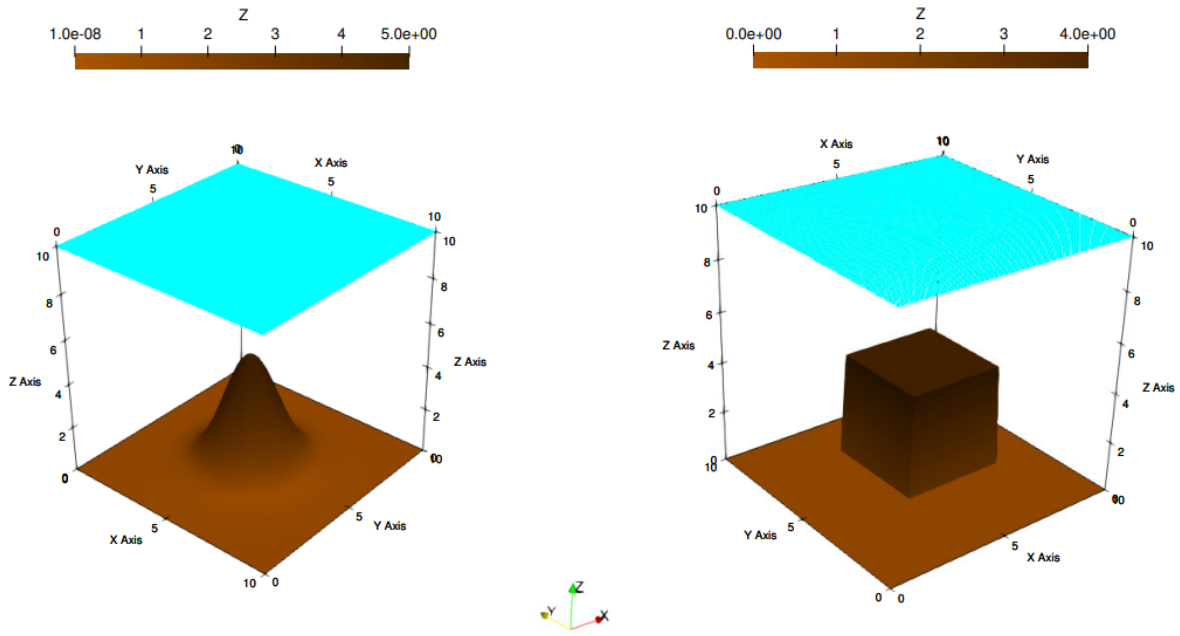

Figure 3: Solution of the well-balancing problem after 1 s of simulation, with the bottom topography defined by $Z_1(\mathbf{x})$ and $Z_2(\mathbf{x}$ respectively.

We summarise the results of the errors computed in the norms $L^1(\Omega)$ and $L^\infty(\Omega)$ in Table 1, both for Z_1 and Z_2, while Figure (3) shows the final time $T = 1\,s$ for the simulations with Z_1 and Z_2, respectively.

Bottom topography: $Z_1(\mathbf{x})$		
State variable	$L^1(\Omega)$	$L^\infty(\Omega)$
h	$2.11e-12$	$3.36e-13$
hu	$1.92e-13$	$2.77e-14$
hv	$2.47e-13$	$3.05e-14$
Bottom topography: $Z_2(\mathbf{x})$		
State variable	$L^1(\Omega)$	$L^\infty(\Omega)$
h	$3.34e-13$	$7.39e-14$
hu	$4.39e-13$	$6.67e-14$
hv	$2.59e-13$	$6.34e-14$

Table 1: Well-balancing test results in $H^1(\Omega)$ and $L^\infty(\Omega)$ norms after 1 s of simulation.

As shown in Table (1), both errors in $L^1(\Omega)$ and $L^\infty(\Omega)$ remain in the order of machine precision. The results obtained verify the well-balancing property of the DAMPM. Furthermore, it should be noted that the formulation presented in (33) allows us to avoid the instabilities that can arise from the gradient of the topography $Z(\mathbf{x})$, since the term $g(h-H)\nabla Z$ vanishes when $h = H$. However, in more realistic landslide situations, the steady state H is usually not easily available and is also difficult to manage. The application of (33) to more complex scenarios requires a more in-depth theoretical study, which goes beyond the scope of this paper.

4.2 Conservation of mass and linear momentum

In Section 3.1.2 we have described the P2G procedure, where the quantities defined on the particles $p \in \{1, ..., N_p\}$ are projected on the grid nodes $i \in \{1, ..., N_v\}$ using the shape functions $N_i(\mathbf{x}_p)$ [38]. The first relation of (20) shows the projection of the linear momentum on the particles $(m\mathbf{v})_p$ on the grid counterpart $(m\mathbf{v})_i$. Since the finite element shape functions N_i make a partition of unity, we have

$$\begin{aligned}\sum_{i=1}^{N_v}(m\mathbf{v})_i &= \sum_{i=1}^{N_v}\left(\sum_{p=1}^{N_p}(m\mathbf{v})_p N_i(\mathbf{x}_p)\right)\\ &= \sum_{p=1}^{N_p}(m\mathbf{v})_p\left(\sum_{i=1}^{N_v}N_i(\mathbf{x}_p)\right)\\ &= \sum_{p=1}^{N_p}(m\mathbf{v})_p.\end{aligned} \tag{36}$$

A similar computation shows that it is also true for the grid mass $\sum_i M_i$ and the particles mass $\sum_p m_p$.

In order to verifying the numerical conservation of mass and linear momentum, we consider the test case defined by the collapse of a material on an inclined orography described by

$$Z(x, y) = 60 - \frac{1}{3}x + 15\exp\left(-\frac{(x-50)^2}{7} - \frac{(y-10)^2}{7}\right) \tag{37}$$

defined on a domain given by $\Omega = [0, 150] \times [0, 20]\, m$. The domain Ω and the collapsing material, a mudflow with density $\rho = 1200\, kg/m^3$, are discretised by 2250 elements and 2100 particles, respectively, resulting in the use of 4 particles per cell. We consider friction, with a viscosity coefficient $\mu = 10\, Pa \cdot s$, a friction angle $\varphi \sim 12°$ and a turbolence coefficient $\xi = 200\, m/s^2$. The total simulation time is set to $T = 3\, s$. The mud, after the sudden collapse due to its

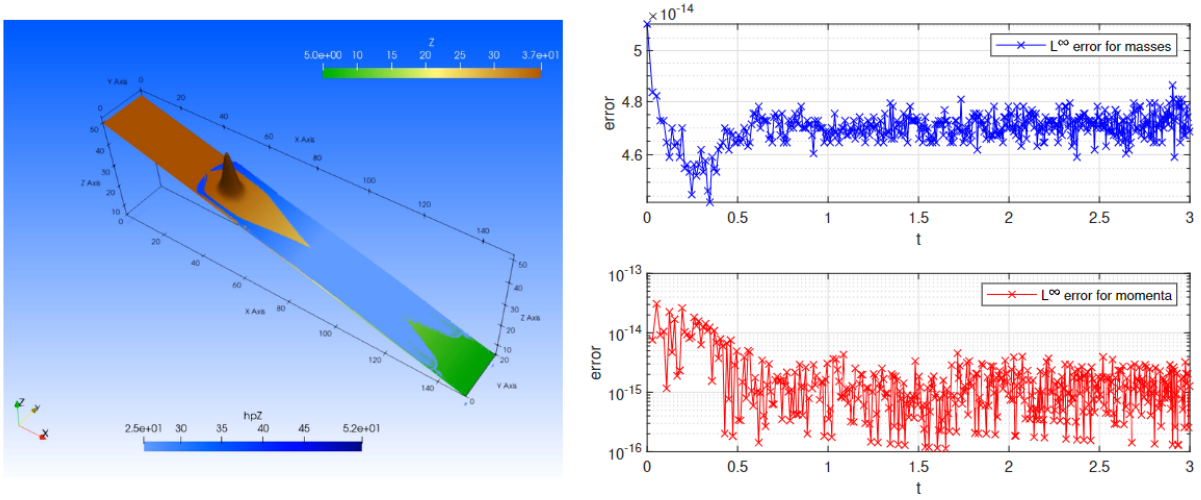

Figure 4: Snapshot of the collapsing material on the bed described by $Z(x, y)$ after $t = 2.5\, s$ of simulation and Trend of the L^∞ error for the momenta and masses conservation between particles and nodes respectively .

weight, the mud starts sliding down the bed until the central obstacle is reached. As shown in Figure 4, after collision with the obstacle, the landslide is split into two symmetric logs that independently continue their slide along the bed until finally reunite. Figure 4 shows even

the infinite norm error of the comparison between the calculated moments and masses on the particles and nodes, respectively. At all time steps of the simulation, the error remains confined to the order of machine precision for both moments $m\mathbf{v}$ and masses m. The test just performed also highlights one of the main advantages of MPM, which is the automatic conservation of mass.

4.3 Application to a real scenario: Bindo-Cortenova landslide

In this section, we consider a real-life test case regarding a landslide phenomenon that occurred in December 2002 near Bindo-Cortenova (LC), a small town in northern Italy. The sliding material consists of large conglomeratic rock blocks, up to 100 m, surrounded by a mixture of sandy gravel. The lower part of the hill experienced a disastrous collapse, involving a substantial volume of approximately 1.2 million cubic metres, after an extended period of exceptionally heavy rain [39].

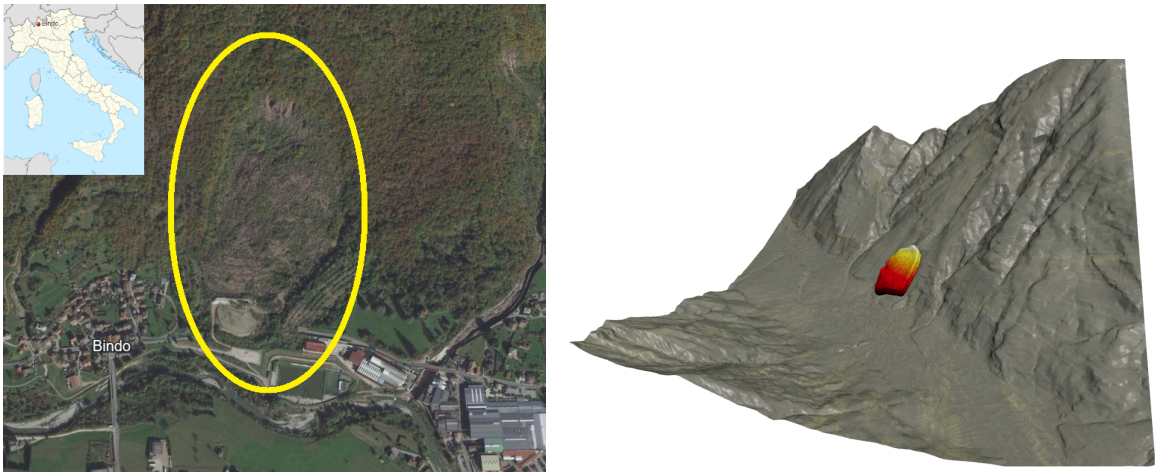

Figure 5: Bindo-Cortenova landslide: on the left panel, the location of the event from a Google Earth image, on the right panel the computational domain of interest and the initial condition.

Before starting with real scenario analysis, it is worth discussing the management of the input data in the computational domain and particle generation in the area of interest.

One of the advantages of MPMs is the relative ease with which data, which often come from digital images (i.e., CT scan, TIFF, or PNG images), can be converted into initial data useful for spatial discretization of the problem analyzed [40, 41, 42]. One of the classical approaches used in the literature is to convert each pixel in the input image into a particle. The characteristic of the material can be deduced, for example, from the pixel color [23]. However, one of the major problems with this approach is related to the resolution of the image itself and consequently to the number of material points used to discretize the initial mass. In the context of landslide simulation, input data on orography and initial conditions on the landslide itself are typically derived from digital terrain models (DTM) generated from satellite interferometric surveys [43, 44, 45]. Once processed, the images are presented in geoTIFF format. The DTM is typically produced in raster format by associating each pixel with the absolute elevation attribute, but the resolution is generally not less than 5 m in spatial extent. Discretizing the initial material by defining a material point for each pixel would generate a configuration with at most a single particle for each cell of the background grid. This process would cause problems in the P2G phase of the method, because for each node $i \in \{1, ..., N_v\}$ of the grid, there would be a mass contribution M_i that would be derived from at most 4 different particles, with the risk of losing information and generating a cell-crossing instability. To avoid this kind of phenomenon, while preserving a sort of independence on the data input, it is sufficient to consider the polygonal

line drawn by the initial condition on the landslide, i.e. its perimeter, and then fill it with a number of particles, regardless of the raster of the input geoTIFF images.

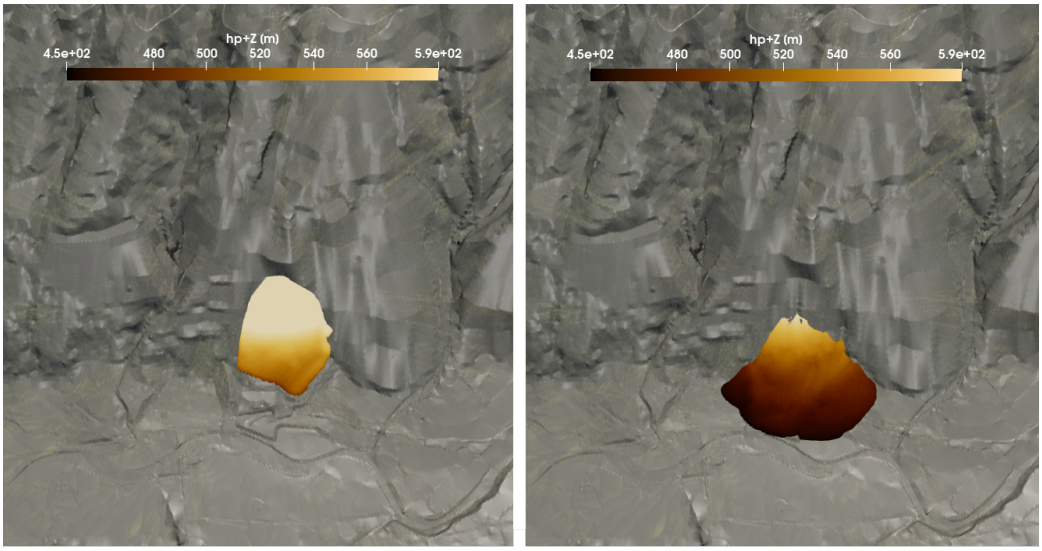

Figure 6: Bindo-Cortenova landslide: two snapshots of the landslide run-out at $t = 2\ s$ and $t = 20\ s$, from left to right respectively.

In our context, the area of interest was discretized from DTM satellite data with a 5-m raster in a domain $\Omega = [0, 1500] \times [0, 1350]\ m^2$ consisting of $5.1 \cdot 10^5$ elements and $6.9 \cdot 10^4$ particles. Following the work done in [39], the initial height of the landslide mass, shown in red on the right panel of Figure 5, is approximately 38 m and lies on a surface inclined about 28° with respect to the horizontal direction, with a residual friction angle φ equals to 34°. Regarding the physical aspects of the event, the material has a density ρ set to 1291 kg/m^3, while the turbulence coefficient ξ, the viscosity μ and the yield shear stress τ_Y are set equal to 200 m/s^2, $2 \cdot 10^3\ Pa$ and 50 $Pa \cdot s$, respectively. The final time is set to $T = 20\ s$. Finally, the problem is complemented by non-reflective boundary conditions.

After sudden triggering, the material collapses along the surface of the hill, following the complex orography of the area, until the toe of the landslide approaches the north bank of the Pioverna river. Figure 6 illustrates the distribution of the material at two different times and the propagation of the front through the intricate local topography.

In Figure 7, the distribution of the main stresses σ^{∇}_{xx} and σ^{∇}_{yy} is depicted at the final instant of the simulation, that is $T = 20\ s$. It can be observed that the pressures along the principal directions peak in the central regions of the landslide material, reaching magnitudes on the order of $2 \cdot 10^5\ Pa$.

The left panel of Figure 8 shows the profile of the domain of interest along the line $x' = 675m$ in which the initial state of the landslide material, with a thickness of about 38 m, and the final state obtained by DAMPM after 20 s of simulation are superimposed, respectively. It can be seen that the total length of the material in the final state is nearly 500 m, compared to the initial length of approximately 400 m, with a maximum height that does not exceed 30 m.

To verify the accuracy of the method, the results of the numerical simulation were compared with the final state of the landslide, obtained from topographic and satellite surveys. The right panel of Figure 8 shows the final state, that is, the scar from the landslide, superimposed on the numerical state, demonstrating that the extent and shape of the region obtained by the DAMPM simulation are consistent with those derived from the surveys. It is important to note that in this case it was considered the general trace left by the landslide during the collapse and not only the final state of motion of each particle, as shown in Figure 6.

A final comparison of the area occupied by each region showed that the difference between

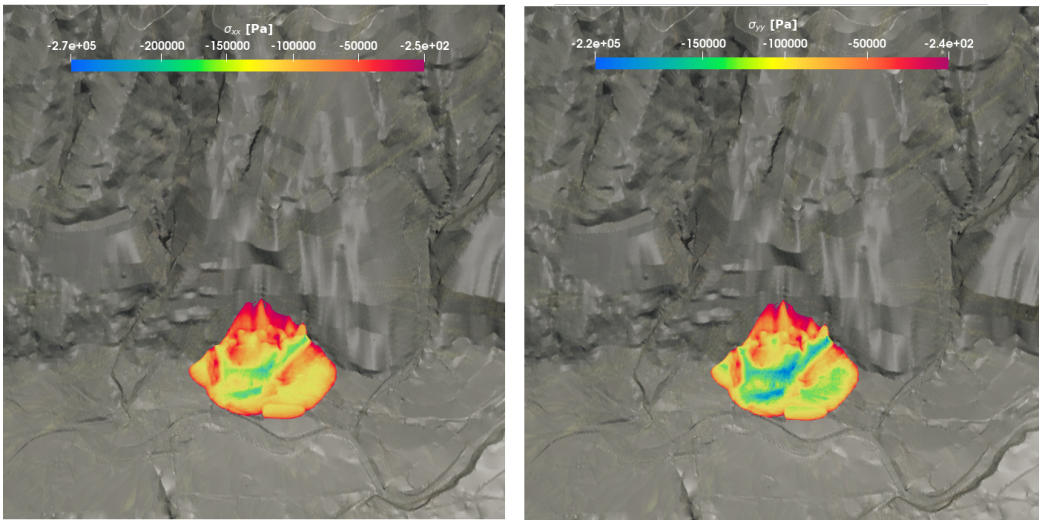

Figure 7: Bindo-Cortenova landslide: distribution of the normal stresses σ_{xx}^{∇} and σ_{yy}^{∇} respectively, after 20 s of simulation.

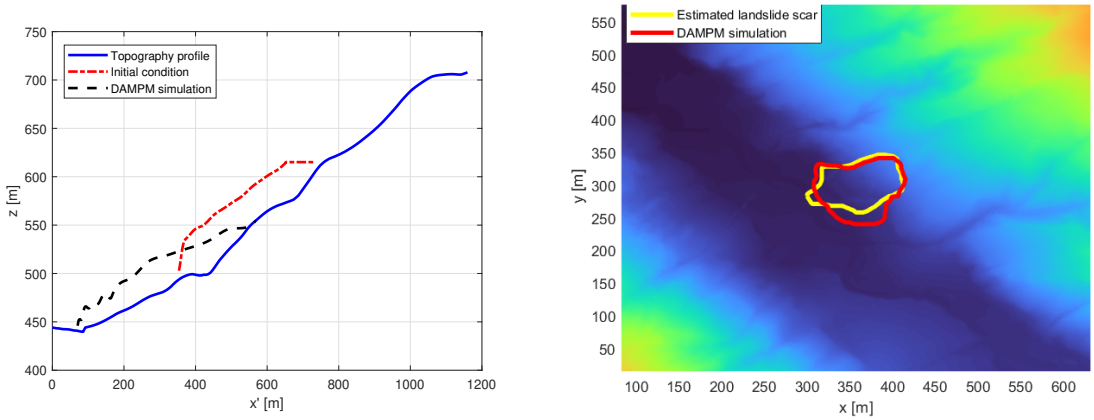

Figure 8: On the left, the profile of the domain of interest, with initial condition (in red) and DAMPM simulation (dotted black line). On the right, the comparison of the total displacement of the Bindo-Cortenova landslide detected numerically and empirically.

the DAMPM simulation and the empirical one is about 16%.

5 Conclusions and perspectives

We proposed a semi-conservative variant of the depth-averaged material point method to solve differential problems dominated by advective control, especially landslide phenomena and mudflows.

We verified the accuracy of the proposed framework with different benchmark tests and showed that, by slightly varying the mathematical formulation of the problem, the method turns out to be well-balanced in the presence of non-flat topographies. We also verified the numerical conservation of masses and momenta between nodes and particles. Finally, we have tested the numerical framework in a real scenario, obtaining coherent and consistent results with respect to the available empirical data.

Modeling landslides or mudflow flow is very challenging, especially in populated areas, and the development of predictive flow tools, in combination with impact analysis models, is an active area of research [15, 46]. For this aim, among the various perspectives on this work,

we mention the enrichment of the presented framework by developing more advanced DAMPM formulations in order to limit stability issues in combination with space-adaptive states. Finally, in order to study and simulate other kind of landslide phenomena, such as debris flows, it would be important to consider multiphase models to take into account both the liquid and solid phases [47].

CRediT authorship contribution statement

Marco Fois - Conceptualization, Investigation, Methodology, Validation, Visualization, Software, Writing – original draft, Writing – review & editing.

Carlo de Falco - Conceptualization, Investigation, Methodology, Validation, Visualization, Software, Supervision, Writing – original draft, Writing – review & editing.

Luca Formaggia - Investigation, Methodology, Project administration, Supervision, Writing – original draft, Writing – review & editing.

Data availability

Data will be made available from the corresponding author upon reasonable request.

Acknowledgements

This research was supported by the Accordo Attuativo ASI-POLIMI "Attività di Ricerca e Innovazione" n. 2018-5-HH.0.

C.d.F. and L.F. also acknowledge the support of "Dipartimento di Eccellenza 2023-2027".

We thank Dr. Monica Corti for providing part of the data for the simulation of the real case study. Politecnico di Milano provided Open Access Funding within the CRUI-CARE agreement.

Conflict of interest

The authors declare that they have no potential conflict of interest.

References

[1] U. Haque, P. F. Da Silva, G. Devoli, J. Pilz, B. Zhao, A. Khaloua, W. Wilopo, P. Andersen, P. Lu, J. Lee, et al., The human cost of global warming: Deadly landslides and their triggers (1995–2014), Science of the Total Environment 682 (2019) 673–684.

[2] U. Haque, P. Blum, P. F. Da Silva, P. Andersen, J. Pilz, S. R. Chalov, J.-P. Malet, M. J. Auflič, N. Andres, E. Poyiadji, et al., Fatal landslides in europe, Landslides 13 (6) (2016) 1545–1554.

[3] M. S. Bernardi, P. C. Africa, C. de Falco, L. Formaggia, A. Menafoglio, S. Vantini, On the use of interferometric synthetic aperture radar data for monitoring and forecasting natural hazards, Mathematical Geosciences 53 (8) (2021) 1781 – 1812.

[4] M. J. Froude, D. N. Petley, Global fatal landslide occurrence from 2004 to 2016, Natural Hazards and Earth System Sciences 18 (8) (2018) 2161–2181.

[5] M. Dilley, Natural disaster hotspots: a global risk analysis, Vol. 5, World Bank Publications, 2005.

[6] F. Gatti, M. Fois, C. de Falco, S. Perotto, L. Formaggia, Parallel simulations for fast-moving landslides: Space-time mesh adaptation and sharp tracking of the wetting front, Int J Numer Meth Fluids 95 (8) (2023) 1286–1309. doi:https://doi.org/10.1002/fld.5186.

[7] K. Abe, K. Konagai, Numerical simulation for runout process of debris flow using depth-averaged material point method, Soils and Foundations 56 (5) (2016) 869–888, special Issue on the International Symposium on Geomechanics from Micro to Macro IS-Cambridge 2014. doi:https://doi.org/10.1016/j.sandf.2016.08.011.

[8] L. Guillet, L. Blatny, B. Trottet, D. Steffen, J. Gaume, A depth-averaged material point method for shallow landslides: Applications to snow slab avalanche release, Journal of Geophysical Research: Earth Surface 128 (8) (2023) e2023JF007092, e2023JF007092 2023JF007092. arXiv:https://agupubs.onlinelibrary.wiley.com/doi/pdf/10.1029/2023JF007092, doi:https://doi.org/10.1029/2023JF007092.
URL https://agupubs.onlinelibrary.wiley.com/doi/abs/10.1029/2023JF007092

[9] D. Sulsky, Z. Chen, H. Schreyer, A particle method for history-dependent materials, Computer Methods in Applied Mechanics and Engineering 118 (1993) 179–196.

[10] D. Sulsky, Erratum: Application of a particle-in-cell method to solid mechanics, Computer Physics Communications (1995).

[11] X. Wang, Y. Qiu, S. R. Slattery, Y. Fang, M. Li, S.-C. Zhu, Y. Zhu, M. Tang, D. Manocha, C. Jiang, A massively parallel and scalable multi-gpu material point method, ACM Trans. Graph. 39 (4) (aug 2020). doi:10.1145/3386569.3392442.
URL https://doi.org/10.1145/3386569.3392442

[12] p. Baioni, T. Benacchio, L. Capone, C. de Falco, Gpus based material point method for compressible flows, in: Particles, 2023.
URL https://www.scipedia.com/public/Baioni_et_al_2023a

[13] P. Dadvand, R. Rossi, E. Oñate, An object-oriented environment for developing finite element codes for multi-disciplinary applications., Arch Computat Methods Eng 17 (2010) 253–297. doi:https://doi.org/10.1007/s11831-010-9045-2.

[14] V. Singer, A. Larese, A. Börst, R. Wüchner, K. Bletzinger, Partitioned mpm-fem coupling approach for advanced numerical simulation of massmovement hazards impacting flexible protective structures., 10th edition of the International Conference on Computational Methods for Coupled Problems in Science and Engineering (2023).

[15] M. V., P. Bucher, R. Zorrilla, R. Rossi, J. Cotela, C. Velázquez, M. Celigueta, J. Maria, T. Teschemacher, C. Roig, M. Maso, G. Casas, S. Warnakulasuriya, M. Núñez, P. Dadvand, S. Latorre, I. de Pouplana, J. González, F. Arrufat, et al., Kratosmultiphysics/kratos: Release 9.2 (v9.2)., Zenodo (2022). doi:https://doi.org/10.5281/zenodo.3234644.

[16] M. Pastor, T. Blanc, B. Haddad, V. Drempetic, M. Mories, P. Stickle, M. Mira, J. Merodo, Depth averaged models for fast landslide propagation: mathematical, rheological and numerical aspects, Archive of Computational Methods in Engineering 22 (2015) 67–104.

[17] M. Quecedo, M. Pastor, M. I. Herreros, J. A. Fernández Merodo, Numerical modelling of the propagation of fast landslides using the finite element method, International Journal for Numerical Methods in Engineering 59 (6) (2004) 755–794. doi:https://doi.org/10.1002/nme.841.

[18] S. Beguería, M. Hees, M. Geertsema, Comparison of three landslide runout models on the turnoff creek rock avalanche, british columbia, in: Landslide Processes Conference: A tribute to Theo van Asch. Strasbourg, 6-7 February, CERG, 2009, pp. 243–247. doi:10.13140/2.1.4569.3767.

[19] R. Sosio, G. Crosta, J. Chen, O. Hungr, Runout prediction of rock avalanches in volcanic and glacial terrains, Landslide Science and Practice: Spatial Analysis and Modelling 3 (2013) 285–291. doi:10.1007/978-3-642-31310-3-38.

[20] M. Mckinnon, O. Hungr, S. McDougall, Dynamic analyses of canadian landslides, Proceedings of the Fourth Canadian Conference on GeoHazards: From Causes to Management (2008) 20–24.

[21] J. I. Finnie, Finite-element methods for free-surface flow, in: M. H. Chaudhry, L. W. Mays (Eds.), Computer Modeling of Free-Surface and Pressurized Flows, Springer Netherlands, Dordrecht, 1994, pp. 115–146. doi:10.1007/978-94-011-0964-2-5.

[22] M. Souli, J. Zolésio, Finite element method for free surface flow problems, Computer Methods in Applied Mechanics and Engineering 129 (1) (1996) 43–51. doi:https://doi.org/10.1016/0045-7825(95)00883-7.

[23] A. de Vaucorbeil, V. P. Nguyen, S. Sinaie, J. Y. Wu, Chapter two - material point method after 25 years: Theory, implementation, and applications, in: S. P. Bordas, D. S. Balint (Eds.), Advances in Applied Mechanics, Vol. 53 of Advances in Applied Mechanics, Elsevier, 2020, pp. 185–398. doi:https://doi.org/10.1016/bs.aams.2019.11.001.

[24] S. Andersen, L. Andersen, Modelling of landslides with the material-point method, Computational Geosciences 14 (2010) 137–147. doi:10.1007/s10596-009-9137-y.

[25] M. Llano, M. Farias, D. Pedroso, An assessment of the material point method for modelling large scale run-out processes in landslides, Landslides 13 (12 2015). doi:10.1007/s10346-015-0664-4.

[26] K. Soga, E. Alonso, A. Yerro, K. Kumar, S. Bandara, Trends in large-deformation analysis of landslide mass movements with particular emphasis on the material point method, Géotechnique 66 (2015) 1–26. doi:10.1680/jgeot.15.LM.005.

[27] F. Harlow, The particle-in-cell computing method for fluid dynamics., Methods in Computational Physics 3 (1964) 319–343.

[28] S. Bardenhagen, E. Kober, The generalized interpolation material point method, CMES - Computer Modeling in Engineering and Sciences 5 (06 2004).

[29] E. Wyser, Y. Alkhimenkov, M. Jaboyedoff, Y. Y. Podladchikov, A fast and efficient matlab-based mpm solver: fmpmm-solver v1.1, Geoscientific Model Development 13 (12) (2020) 6265–6284. doi:10.5194/gmd-13-6265-2020.

[30] A. Sadeghirad, R. M. Brannon, J. Burghardt, A convected particle domain interpolation technique to extend applicability of the material point method for problems involving massive deformations, International Journal for Numerical Methods in Engineering 86 (12) (2011) 1435–1456. arXiv:https://onlinelibrary.wiley.com/doi/pdf/10.1002/nme.3110, doi:https://doi.org/10.1002/nme.3110.

[31] A. Stomakhin, C. Schroeder, L. Chai, J. Teran, A. Selle, A material point method for snow simulation, ACM Trans. Graph. 32 (4) (jul 2013). doi:10.1145/2461912.2461948.

[32] P. Wallstedt, J. Guilkey, An evaluation of explicit time integration schemes for use with the generalized interpolation material point method, Journal of Computational Physics 227 (2008) 9628–9642. doi:10.1016/j.jcp.2008.07.019.

[33] S. Bardenhagen, Energy conservation error in the material point method for solid mechanics, Journal of Computational Physics 180 (2002) 383–403. doi:10.1006/jcph.2002.7103.

[34] B. Rogers, M. Fujihara, A. G. L. Borthwick, Adaptive q-tree godunov-type scheme for shallow water equations, International Journal for Numerical Methods in Fluids 35 (3) (2001) 247–280. doi:https://doi.org/10.1002/1097-0363(20010215)35:3¡247::AID-FLD89¿3.0.CO;2-E.

[35] B. D. Rogers, A. G. Borthwick, P. H. Taylor, Mathematical balancing of flux gradient and source terms prior to using roe's approximate riemann solver, Journal of Computational Physics 192 (2) (2003) 422–451. doi:https://doi.org/10.1016/j.jcp.2003.07.020.

[36] F. Gatti, C. de Falco, S. Perotto, L. Formaggia, A scalable well-balanced numerical scheme for the simulation of fast landslides with efficient time stepping, Applied Mathematics and Computation 468 (2024) 128525. doi:https://doi.org/10.1016/j.amc.2023.128525.

[37] Y. Xing, C. Shu, A new approach of high order well-balanced finite volume weno schemes and discontinuous galerkin methods for a class of hyperbolic systems with source terms, Communications in Computational Physics 1 (1) (2006) 100–134. doi:10.1016/j.jcp.2005.10.005.

[38] D. Burgess, D. Sulsky, J. Brackbill, Mass matrix formulation of the flip particle-in-cell method, Journal of Computational Physics 103 (1) (1992) 1–15. doi:https://doi.org/10.1016/0021-9991(92)90323-Q.

[39] M. Secondi, G. Crosta, G. Frigerio, P. Frattini, F. Agliardi, Landslide Motion Forecasting by a Dynamic Visco-Plastic Model, Vol. 3, 2013, pp. 151–160. doi:10.1007/978-3-642-31310-321.

[40] J. Guilkey, J. Hoying, W. J., Computational modeling of multicellular constructs with the material point method., J Biomech. 39(11) (2006) 2074–2086. doi:10.1016/j.jbiomech.2005.06.017.

[41] S. Bardenhagen, A. Brydon, J. Guilkey, Insight into the physics of foam densification via numerical simulation, Journal of the Mechanics and Physics of Solids 53 (3) (2005) 597–617. doi:https://doi.org/10.1016/j.jmps.2004.09.003.

[42] J. Nairn, Material point method simulations of transverse fracture in wood with realistic morphologies, Holzforschung 61 (06 2007). doi:10.1515/HF.2007.057.

[43] M. Xie, W. Zhao, N. Ju, C. He, H. Huang, Q. Cui, Landslide evolution assessment based on insar and real-time monitoring of a large reactivated landslide, wenchuan, china, Engineering Geology 277 (2020) 105781. doi:https://doi.org/10.1016/j.enggeo.2020.105781.

[44] L. Brocca, F. Ponziani, T. Moramarco, F. Melone, N. Berni, W. Wagner, Improving landslide forecasting using ascat-derived soil moisture data: A case study of the torgiovannetto landslide in central italy, Remote Sensing 4 (5) (2012) 1232–1244. doi:10.3390/rs4051232.

[45] S. Mirzaee, M. Motagh, B. Akbari, Landslide monitoring using insar time-series and gps observations, case study: Shabkola landslide in northern iran, The International Archives of the Photogrammetry, Remote Sensing and Spatial Information Sciences XLII-1/W1 (2017) 487–492. doi:10.5194/isprs-archives-XLII-1-W1-487-2017.

[46] S. Cuomo, A. Di Perna, M. Martinelli, Design Protection Barriers Against Flow-Like Landslides, Springer International Publishing, Cham, 2023, pp. 123–136. doi:https://doi.org/10.1007/978-3-031-16898-7_8.

[47] F. Gatti, C. de Falco, S. Perotto, L. Formaggia, M. Pastor, A scalable well-balanced numerical scheme for the modeling of two-phase shallow granular landslide consolidation, Journal of Computational Physics (2024) 112798doi:https://doi.org/10.1016/j.jcp.2024.112798.

MOX Technical Reports, last issues

Dipartimento di Matematica
Politecnico di Milano, Via Bonardi 9 - 20133 Milano (Italy)

16/2024 Domanin D. A.; Pegoraro M.; Trimarchi S.; Domanin M.; Secchi P.
Persistence diagrams for exploring the shape variability of abdominal aortic aneurysms

14/2024 Zappon, E.; Salvador, M.; Piersanti, R.; Regazzoni, F.; Dede', L.; Quarteroni, A.
An integrated heart-torso electromechanical model for the simulation of electrophysiological outputs accounting for myocardial deformation

15/2024 Vaccaro, F.; Mauri, A.G.; Perotto, S.; Brivio, S.; Spiga, S.
Modeling and simulation of electrochemical and surface diffusion effects in filamentary cation-based resistive memory devices

12/2024 Zingaro, A.; Ahmad, Z.; Kholmovski, E.; Sakata, K.; Dede', L.; Morris, A.K.; Quarteroni, A.; Trayanova, N.A.
A comprehensive stroke risk assessment by combining atrial computational fluid dynamics simulations and functional patient data

Antonietti, P.F.; Corti, M.
Numerical modelling of protein misfolding in neurodegenerative diseases a computational study

11/2024 Antonietti, P.F.; Corti, M.
Numerical modelling of protein misfolding in neurodegenerative diseases: a computational study

09/2024 Leimer Saglio, C. B.: Pagani, S.; Corti, M.; Antonietti, P. F.
A high-order discontinuous Galerkin method for the numerical modeling of epileptic seizures

10/2024 Capuano E.; Regazzoni F.; Maines M.; Fornara S.; Locatelli V.; Catanzariti D.; Stella S.; Nobile F.; Del Greco M.; Vergara C.
Personalized Computational Electro-mechanics Simulations to Optimize Cardiac Resynchronization Therapy

05/2024 Conti, P.; Gobat, G.; Fresca, S.; Manzoni, A.; Frangi, A.
Reduced order modeling of parametrized systems through autoencoders and SINDy approach: continuation of periodic solutions

06/2024 Antonietti, P.F., Bonetti, S., Botti, M., Corti, M., Fumagalli, I., Mazzieri, I.
lymph: discontinuous poLYtopal methods for Multi-PHysics differential problems